Epitaxial graphene on 6*H*-SiC(0001): Defects in SiC investigated by STEM

Markus Gruschwitz,[1] Herbert Schletter,[1] Steffen Schulze,[1] Ioannis Alexandrou,[2] and Christoph Tegenkamp[1,*]
[1]*Institut für Physik, Technische Universität Chemnitz, Reichenhainer Str. 70, 09126 Chemnitz, Germany*
[2]*Thermo Fisher Scientific, Achtseweg Noord 5, 5651 GG Eindhoven, The Netherlands*

(Received 22 July 2019; published 17 September 2019)

The continuous improvement of the sublimation process of SiC allows using epitaxial graphene nowadays for quantum metrology. While it is known that the interface between graphene and the SiC surface is crucial for graphene's transport properties, almost no information about the composition of the SiC substrate *after* the sublimation process is available. In this study we present high resolution c_s-corrected scanning transmission electron microscopy (STEM) experiments on 6*H*-SiC(0001) samples after growth of graphene. A Si deficiency within the first three SiC bilayers was found by atomically resolved energy dispersive x-ray spectroscopy (EDX). The Si concentration within the first bilayer can be reduced up to 50%. In addition, as probed by electron energy loss spectroscopy, the hybridization state of C within the first five bilayers revealed a sp^2 contribution, which we refer to as the precipitation of small carbon clusters. Our analysis clearly shows that the electronic interface of epitaxial graphene on 6*H*-SiC(0001) is not atomically sharp.

DOI: 10.1103/PhysRevMaterials.3.094004

I. INTRODUCTION

The 2D material graphene has sparked a lot of interest due to its outstanding mechanical, electrical, and optical properties [1,2] and triggers intense research towards the growth of perfect graphene layers. There are numerous recipes reported for the growth of epitaxial graphene [3,4]. For instance, the thermal decomposition of hydrocarbon gases on transition metal surfaces like Ir(111) or Pt(111) surfaces is a self-limiting decomposition process and results in the growth of long-range ordered monolayer structures [5,6]. The catalytic activity of the surface is important and substrate steps are overgrown. These concepts were successfully upscaled allowing us to grow continuously using Cu foil on rotating cylinders on square meter scales [7]. However, subsequent transfer techniques are needed if the graphene is intended to be used for electronic applications. Therefore, direct growth of graphene on semiconducting substrates is appealing. For instance, by means of chemical vapor deposition (CVD) or molecular beam epitaxy (MBE), graphene monolayers were successfully grown on Ge(001) [8–10].

In contrast, the growth of graphene on SiC(0001) succeeds simply by heating without the need of any external carbon sources. At high temperatures the vapor pressure of Si, compared to C, is higher by four orders of magnitude and sufficient to grow graphene layers on top [11]. However, it was immediately realized that the SiC surface structure plays a crucial role. Compared to metal supports, step edges or dislocations in SiC give rise to graphene bilayer formation [12,13]. In order to further minimize the influence of these SiC imperfections towards an homogeneous sublimation across the surface, the high temperature treatment of SiC is performed in a high pressure background of an Ar atmosphere [14]. The subsequent optimization of this process, i.e., tuning the gas flow within the reactor or using resist-based techniques, results in an almost perfect growth where substrate defects are continuously overgrown by monolayer graphene [15,16].

Most of the research done so far on the growth of graphene on SiC inherently assumes that the host material remains structurally and stoichiometrically intact [17–22]. As the graphene/SiC heterostructure resembles a Schottky structure [23], thus not only the interface between the graphene and SiC-surface but also the near-surface region of the SiC is important for the functionality of this heterostructure. Indeed, both from a thermodynamic and kinetic point of view, an atomically sharp interface between epitaxial graphene and SiC(0001) is unlikely. At sublimation temperatures far above 1500 K, the vapor pressures for molecular species (e.g., SiC_2 and Si_2C) are not negligible [11]. Moreover, diffusion processes at these high temperatures should affect the stoichiometry of the SiC crystal close to the surface also.

In a previous scanning transmission electron microscopy (STEM) study contrast changes across the surface detected with the high angle annular dark field detector (HAADF) were explained by variation of the silicon concentration [24]. Moreover, from recent x-ray reflectivity and x-ray standing wave measurements, a Si deficiency of 25% within the first SiC layer was reported [25]. Although there are indications for nonstoichiometry effects, detailed high-resolution TEM measurements, which easily can resolve such imperfections, have not been reported so far.

In this paper we present energy dispersive x-ray (EDX) and electron energy loss spectroscopy (EELS) conducted in a scanning transmission electron microscope (STEM) with atomic resolution across the graphene/6*H*-SiC(0001) interface. Being aware of the fact that a near-surface thinning during preparation of the TEM lamella with focused ion beam (FIB) can also mimic apparent degradation effects, we carefully checked the thickness variation. As a result, a

*christoph.tegenkamp@physik.tu-chemnitz.de

gradual depletion of Si towards the surface across the first three bilayers (0.75 nm) was found. Moreover, by analyzing the hybridization state, we observe that a modification of the sp^3 hybridization of the C atoms within SiC started already 1.25 nm below the surface. Based on a simple model we propose that graphitic clusters of sp^2-hybridized C atoms are embedded close to the surface.

II. EXPERIMENTAL DETAILS

Epitaxial graphene layers were fabricated by thermal annealing of 6*H*-SiC(0001) substrates using the so-called face-to-face method heating the samples up to 1800 K [26]. Besides monolayer graphene samples, also bilayer structures were analyzed in this study.

Lamella structures of the graphene/SiC(0001) samples for cross-sectional scanning transmission electron microscopy (STEM) were prepared utilizing different focused ion beam (FIB) systems (Helios G4 UC and Scios 2 dual beam) both using Ga ion sources. Prior to the FIB preparation, the samples were coated with an approximately 200 nm thick layer of amorphous carbon followed by the deposition of a 2 μm thick layer of platinum. The STEM lamellas were cut out with a thickness of a few microns. Electron transparency was finally reached by thinning the lamellas down to about 30 nm around the interface area by subsequently using ions of 30 keV, 5 keV, and 2 keV for polishing under an angle of approximately 1°. The resulting thickness and smoothness of the lamella were controlled by EELS, EDX, and atomic force microscopy (AFM) (see below).

The samples were characterized in detail by means of a double c_s-corrected STEM (ThemisZ) operating for our studies at a primary electron energy of 80 keV in order to prevent knock-on damage in the graphene films and SiC substrate [27,28]. With an X-FEG field emission gun and a monochromator the electron energy spread was 0.2 eV. X-ray detection was done in STEM mode with a four segment EDX detector.

Atomic resolution in EDX scans was achieved by focusing the electron beam down to 0.2 nm in diameter at a current of 100 pA. The STEM system contains also a Gatan Enfinium spectrometer for EELS. The prominent losses (zero loss peak, Si-L edge, C-K edge) were recorded simultaneously. For both EELS and EDX, spectrum images were recorded by acquiring complete spectra for every pixel while scanning over a two-dimensional region of interest. 1D plots of spectral intensities were made afterwards by averaging the spectra along the SiC(0001) planes ([11$\bar{2}$0] direction) resulting in line scans across the SiC-graphene interface.

III. RESULTS AND DISCUSSION

A. Structural data: Scanning TEM

Figure 1 shows a high resolution cross section STEM image of bilayer graphene on 6*H*-SiC(0001). The transmitted signal was detected by the HAADF, thus the white contrast in the lower part of the image shows the Si atoms of the SiC lattice. The micrograph was calibrated by the bilayer distance in the substrate which amounts to 251 pm [29].

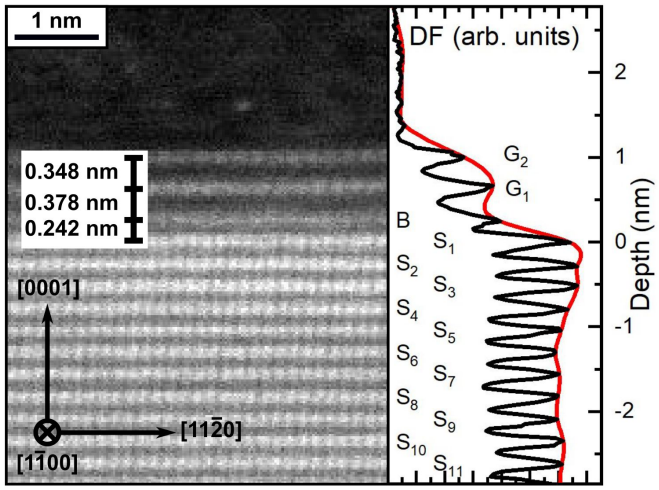

FIG. 1. STEM-HAADF image of an epitaxial bilayer graphene on 6*H*-SiC(0001). The distances between the carbon layers and to the substrate are denoted. The layers are labeled with G_n for graphene, B for buffer layer, and S_n for substrate bilayers counted from the interface. The averaged HAADF signal is shown to the right. The envelope shows an increased HAADF intensity of the five bilayers closest to the interface. The depth scale is given with respect to the topmost SiC bilayer.

The graphene-related layer distances at the surface can be measured with high accuracy and are denoted in Fig. 1. Due to the weak waviness of the carbon layer the values were averaged over multiple measurements. The distance between the topmost two carbon layers is close to the graphite interlayer distance of 335 pm. Taking this value as a reference, the distance between the topmost SiC bilayer and the first carbon layer is considerably reduced, while the distance between the first and second carbon layer is increased. Both deviations can be explained by the formation of a carbon buffer layer. Unsaturated bonds at the SiC(0001) substrate surface induce covalent bonds to the first carbon layer. Therefore, part of the atoms in this first carbon layer (buffer layer) are sp^3 hybridized resulting in an increased bond strength and thus decreased distance to the substrate surface. This partial sp^3 hybridization of the buffer layer decreases the amount of π orbitals and thus reduces the π-π bonding between the buffer and first graphene layer leading to an increased layer distance.

These deviations of the graphene layer distances (compared to graphite) are in accordance with comparable (S)TEM, STM, and XPS measurements. For the SiC-buffer layer distance, experimental values of 197 pm [30], 200 pm [31], 230 pm (4*H*-SiC) [32], and 250 pm (4*H*-SiC) [33] are reported, which are close to values obtained by density functional theory, 258 pm [34]. An increased distance between the buffer and first graphene layer was reported also by Weng *et al.* together with a decreased substrate-buffer distance [24]. Similar results are obtained for 4*H*-SiC [25,35,36].

Along the [1$\bar{1}$00] direction (direction of incidence) the periodicity of the 6H polytype is not visible. Only the modulation of the HAADF signal, faintly visible by the red line in the right of Fig. 1, shows a three bilayer periodic modulation, i.e., half of the 6H unit cell. Moreover, the integrated signal

of the top five bilayers within the SiC is increased, i.e., the electron backscattering rate is higher in this area. A thinning of the lamella would cause the opposite behavior. We will demonstrate in the following that this effect is a result of stoichiometric modifications and carbon precipitates rather than by a geometric thickness variation of the lamella. Despite this increase of the HAADF intensity close to the surface, the STEM contrast conveys the impression of a perfect SiC lattice.

B. Spectroscopic data: EDX and EELS

EDX and EEL spectroscopy were performed in order to characterize the compositional and electronic properties of the near-surface layers. The spectra of both signals were recorded simultaneously, thus can be directly correlated with each other. The corresponding STEM micrographs in dark field (DF) and integrated differential phase contrast (iDPC) mode are shown in Figs. 2(a) and 2(b) [37].

Figure 2(c) shows the EDX spectrum integrated over the entire sample area (size $\approx 1.5 \times 3$ nm^2). The most intense peaks originate from the K edges of Si and C. The other intense peaks can be assigned to O and Cu emissions stemming from the transfer of the sample to the STEM system under ambient conditions and the sample holder, respectively. Less intense emissions, as labeled in the inset, originate from deflected electron excitations from the sample chamber and the Pt protective layer as well as from Ga ions implanted into the sample surface during the FIB sample preparation.

In Fig. 2(d) we show EELS spectra taken at various positions. In order to increase the signal-to-noise ratio, the spectra were averaged along the [11$\bar{2}$0] direction over a spatial window of approximately 1.5 nm at different positions across the lamella structure. The positions are marked in Fig. 2(a). The spectra reveal two main loss features at the C-K edge: The loss at approximately 287 eV refers to the 1s $\rightarrow$ π^* transition, while the loss at around 293 eV is assigned to the 1s $\rightarrow$ σ^* transition as well as transitions into higher π and σ orbitals. [35]. The appearance of these losses comes along with the presence of π and σ bonds in carbon and, hence, is indicative for sp^2 hybridization, as in graphene, or a sp^3 hybridization like for C in SiC. For the spectrum taken in SiC only the σ^* transition is seen. On the contrary, in graphene the π^* transition shows maximum intensity. The SiC spectrum taken closer to the interface already shows significant modifications in the windows of the σ^* and π^* losses. A more detailed analysis will be presented in the following.

C. EELS and EDX mappings: Near-surface substrate composition

Based on the spectral fingerprint features presented in the previous section, maps of the chemical composition as well as the electronic configuration of the graphene/SiC interface were taken and analyzed in more detail. The averaged EDX emissions across the interface structure for C and Si are shown in Fig. 3(b) together with the intensity variation from the DF detector. The maxima of the Si EDX signal coincide with those of the DF intensity, showing the atomic resolution of

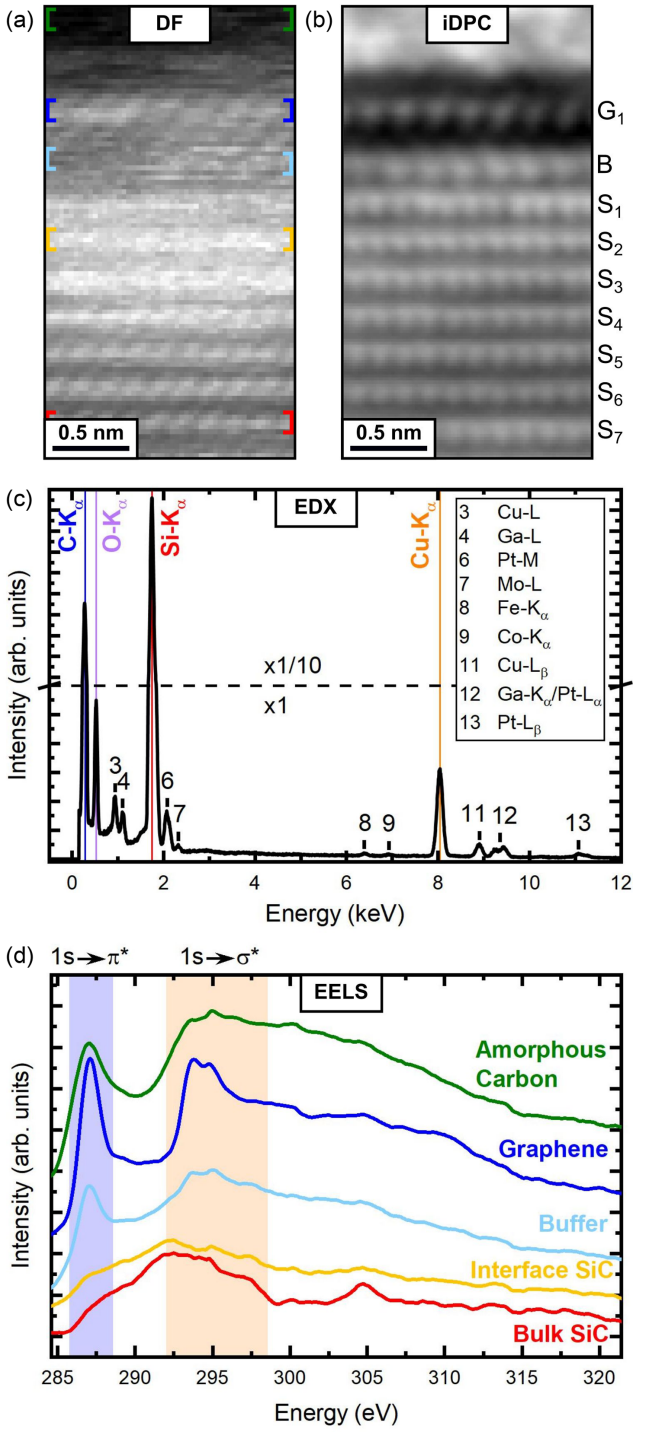

FIG. 2. (a) DF field image of monolayer graphene on 6*H*-SiC(0001). (b) Differential phase contrast (iDPC) image of the same sample revealing a better signal to noise ratio compared to the DF image. (c) Characteristic EDX overview spectrum revealing the elements from the sample and sample holder. (d) EELS spectra, being averaged over small horizontal stripes of same color, as marked in (a). The spectra in (c) and (d) were deduced from the spectrum images taken simultaneously with the DF image in (a).

the spectroscopic mode of operation. Clear maxima of the Si-EDX signals are detected for each SiC bilayer. Figure 3(b) reveals a finite Si intensity is detected also at the position

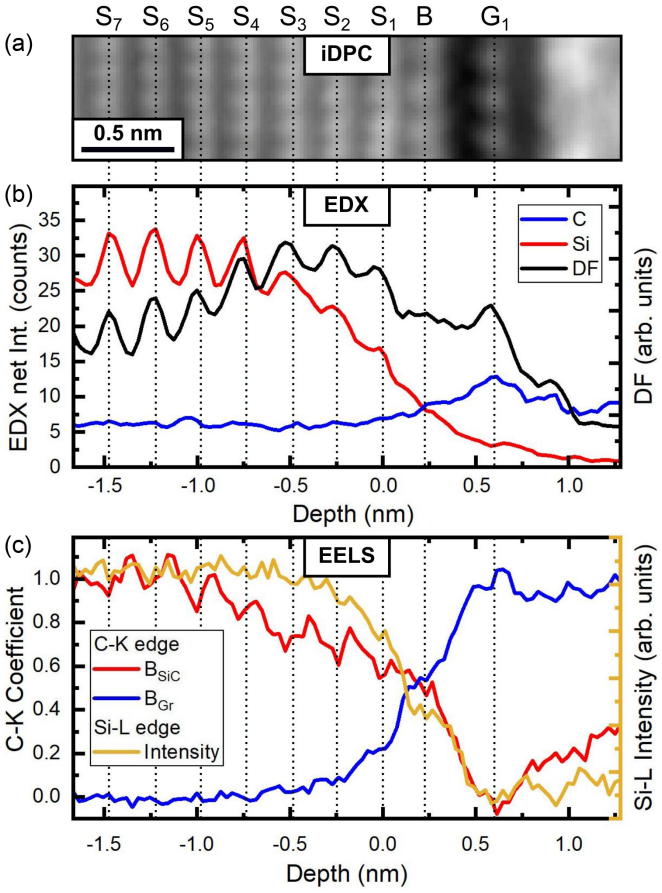

FIG. 3. EDX and EELS analysis of the interface area. (a) Differential phase contrast (iDPC) image of the region of interest. (b) EDX data: net intensities of the silicon and carbon EDX peaks together with a line scan of the DF intensity of (a); (c) EELS data: MLLS coefficients for C-K edge (comprising the sp^3 hybridized SiC-type and the sp^2 hybridized graphene type) and the integrated Si-L edge intensity. All signals were recorded simultaneously during the scan. Line scans were generated by horizontal averaging of the original 2D spectrum image.

of the buffer layer, which we attribute to concomitant EDX signal from adjacent SiC layers due to scattered electrons. This parasitic effect is limiting the EDX resolution. However, despite the agreement in the peak positions, the intensity of both signals behaves significantly different. As already mentioned in the context of Fig. 1, the DF intensity increases towards the interface with an abrupt decrease after the topmost SiC layer. The increased DF intensity arises from Si vacancies, which may induce strain fields in the vicinity of these defect sites [24,38]. Indeed, the presence of such Si vacancies is in line with the Si EDX measurements. As we will discuss in detail below, we can assume a homogeneous thickness of the lamella structure in this area, thus the decrease in Si-EDX signal indicates a compositional effect. The C-EDX signal shows a clear maximum only at the position of graphene. Albeit the cross section for C is only marginally lower compared to Si, the lattice periodic modulation of the C signal is not apparent. We attribute the increase of the C-EDX intensity inside the substrate close to the interface to carbon precipitates formed in the area close to the surface.

As mentioned, the carbon hybridization strongly influences the shape of the C-K edge. In order to quantify the hybridization states a multiple linear least square (MLLS) fit was used to compose each spectrum from the reference spectra for graphene and SiC (S_{Gr} and S_{SiC}) taken from the blue and red stripes in Fig. 2(a) and shown in Fig. 2(d) via $F(E) = AE^{-r} + B_{SiC}S_{SiC}(E) + B_{Gr}S_{Gr}(E)$, where AE^{-r} describes the background (power law function) and B_{SiC} and B_{Gr} the weighting factors of the reference spectra [39]. Figure 3(c) shows the B_i coefficients across the interface. Most importantly, the B_{SiC} component, which is a measure of the sp^3 hybridization of the C within the SiC matrix, is decreased within the last 5 bilayers of SiC.

In order to further quantify the Si depletion in the SiC substrate, the Si-L edge in the EEL spectra at 99 eV was analyzed [cf. Fig. 3(c)]. The Si-L edge was recorded as part of the low loss spectrum, i.e., a comparably short acquisition time has been used leading to a bad signal to noise ratio for the Si-L edge. However, it should be noted that also the Si-EELS signal appears modulated from adjacent layers, thus is nonzero at the position of the buffer layer. In contrast to C, the fine structure of this edge remains the same because the atomic state does not change, thus we plotted directly an averaged Si-L signal. Its intensity is directly proportional to the Si concentration and therefore the depth from the interface.

The combined EDX and EELS information provides insight into the substrate structure near the surface. The first change can be observed at the depth of five bilayers in the form of a B_{SiC} decrease. Without the elemental concentration changing, this points towards defects in the crystal structure influencing the bonding types such as antisites. For the S_3 bilayer, a decreasing of the Si-EDX intensity indicates the presence of Si vacancies. Due to the high process temperature, diffusion of atoms from this layer to the surface is likely. Both Si-EDX and Si-L edge intensity decrease further towards the surface. The higher defect density leads to local carbon rearrangements in the form of graphitic clusters resulting in an increased amount of sp^2 hybridized C atoms. These clusters grow in size until a complete layer of graphitelike carbon is formed, i.e., the buffer layer B. At this layer a mixture of sp^2 and sp^3 hybridized C atoms is measured due to the strong backbonding to the substrate. In the first graphene layer the B_{SiC} instantly drops to zero.

D. Quantitative determination of the SiC stoichiometry and composition

For a quantitative determination of the Si deficiency and surface-near composition of the SiC, details of inelastic mean free path length (IMPF, λ) across the interface are important. In general, the IMFP with respect to the sample thickness t can be deduced from an EEL spectrum via $t/\lambda = \ln(I_t/I_{ZLP})$, where I_t denotes the total integral intensity of the complete spectrum and I_{ZLP} refers to the integral intensity of the zero loss peak [40]. The obtained t/λ ratio across the interface is shown in Fig. 4. We will show in the following that a considerable decay of this ratio is caused by changes of the inelastic mean free path λ rather than by changes in the sample thickness t. The overall decay is superimposed by a

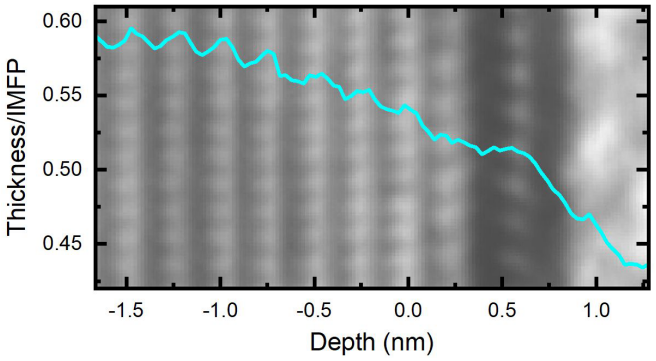

FIG. 4. Thickness/IMFP plot across the graphene/SiC interface. For better orientation, the background shows the DPC image of the region of interest.

modulation of the atomic lattice, which almost vanishes closer to the interface.

Due to the etching and polishing steps, the TEM lamella not necessarily provides parallel and smooth surfaces. An SEM image of the TEM lamella is shown in Fig. 5(a). Besides checking the widths of the lamella at the top and bottom with SEM, we also performed an extended SEM-based EDX thickness mapping using the Si-K line. The k ratio of Si-K$_\alpha$ line, which is the ratio of the line intensities from the thin lamella and from a bulk SiC sample, was measured and compared

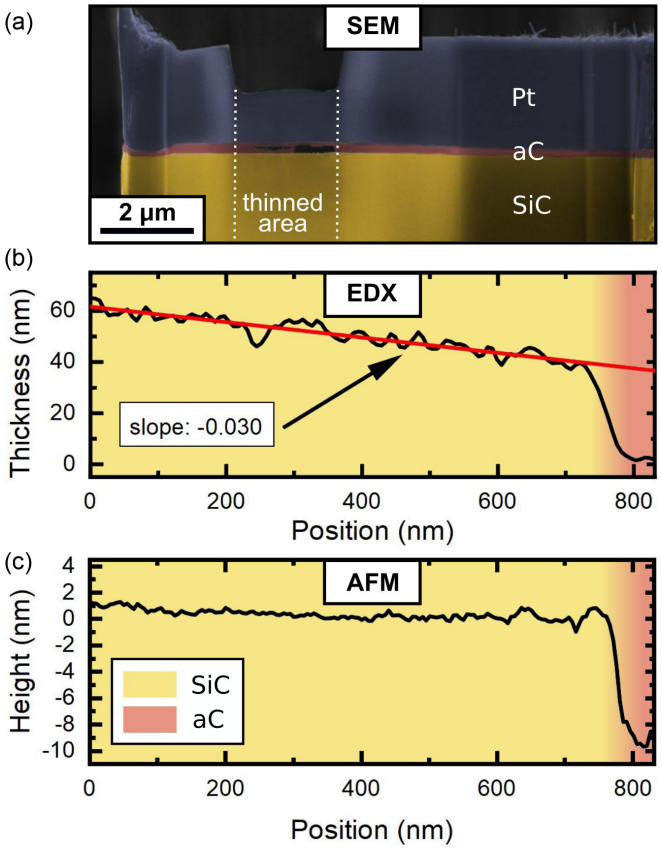

FIG. 5. Structural analysis of the TEM lamella fabricated by FIB. (a) Colored SEM image of the lamella. (b) Thickness versus position across the interface deduced from SEM/EDX measurements [41]. (c) AFM profile taken also across the TEM lamella.

with calculations from a thin film calculation using the so-called ZAF correction method taking into account the atomic number Z, the absorption A, and fluorescence F [41,42]. A line scan of the thickness profile across the interface is shown in Fig. 5(b) showing that the thickness of the lamella is constant within 1–2° of miscut. Moreover, we investigated the lamella also by means of AFM. The lamella provide a small height difference of around 0.4 nm between the substrate and the area where the deposited amorphous carbon starts. This step originates most likely from the ion etching process. At the transition from a material with a low etching rate (SiC) to a material with a higher etching rate (amorphous carbon) underetching occurs. A more detailed localization and imaging of the step is limited by the AFM tip shape. Extended exposure times in the STEM result in significant knock on damage, as can be seen in Fig. 5(a) (black hole in center of the lamella). The line scan in Fig. 5(c) is taken around this damage and reveals a somewhat higher step. The roughness of the lamella surface amounts to around 200 pm demonstrating that the FIB processing was quite noninvasive. Based on these findings, we conclude that the strong decay of the t/λ ratio is caused by changes of the inelastic mean free path λ rather than that of the sample thickness t.

Generally, the IMFP depends on the particle density n and the cross section for inelastic scattering σ of a material, $\lambda = (n\sigma)^{-1}$. Since the particle density can be expressed as $n = \rho N_A/A$, with mass density ρ, atomic mass A, and the Avogadro constant N_A, the IMFP finally reads

$$\lambda = A/(N_A \sigma \rho). \tag{1}$$

For a diatomic compound, A and σ can be expressed by their components. Considering stoichiometric defects in SiC, i.e., Si$_x$C with the atomic fraction $0 \leqslant x \leqslant 1$, we can write for the atomic mass and cross section $A = A_C + x \cdot A_{Si}$ and $\sigma = \sigma_C + x \cdot \sigma_{Si}$, respectively. Values for the cross sections for inelastic scattering were deduced from the IMFP of SiC by using the empirical formula given by Malis *et al.* [43]. For measurements at 80 keV these amount to $\sigma_C \approx 1.44 \times 10^{-4}$ nm^2 and $\sigma_{Si} \approx 1.8 \cdot \sigma_C$.

In order to determine λ for nonstoichiometric SiC, a suitable model for the mass density ρ needs to be derived. In Fig. 6(a) the mass density of Si$_x$C as a function of the Si content x is plotted under three different scenarios: First, assuming that Si vacancies remain on their lattice sites the mass density of Si$_x$C will fall below that of graphite around $x = 0.5$ (gray line). Second, in case the Si vacancies are refilled by C atoms, the critical fraction value is at $x \approx 0.25$ (red line). For the third and most likely scenario we assume that the density of Si$_x$C needs to be larger than that of graphite, because graphene layers are formed at this density. At the high growth temperatures, the surface-near area will most likely undergo a phase separation, i.e., locally the substrate still reveals stoichiometric SiC and C precipitates. The gradual increase of the sp^2 hybridization deduced from the C-K edge EELS signal [cf. B$_{Gr}$ component in Fig. 3(c)] suggests that these clusters are graphiticlike with sp^2-hybridized C atoms. Moreover, as clusterlike structures were not found by STEM, we assume very small clusters of a few nanometers size only. Regardless of their inner structure such small clusters would not be visible in a monocrystalline specimen of 30 nm

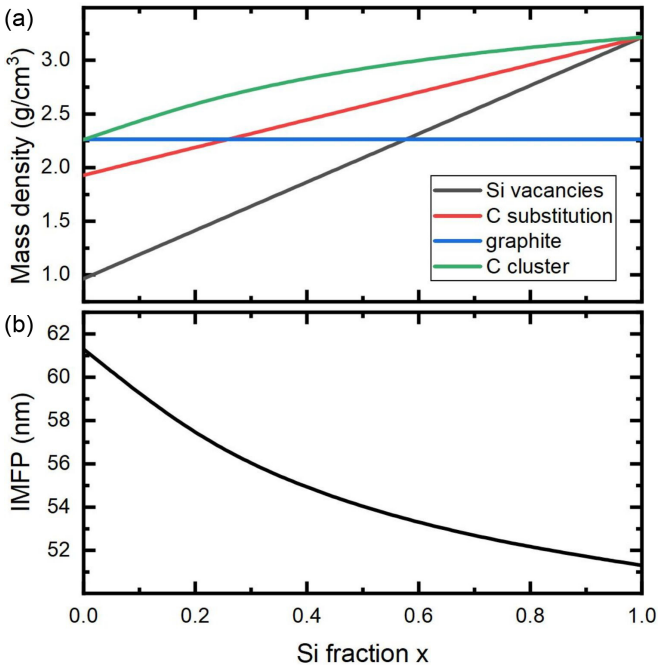

FIG. 6. (a) Mass densities as a function of x in Si_xC for three different microstructure models: remaining vacancies on the vacation of Si-sites (gray), replacement of the vacancies by C atoms, phase separation between SiC and graphite-like inclusions (green). (b) Calculated inelastic mean free path λ for 80 keV electrons in Si_xC as a function of the Si fraction x.

thickness. In order to model $\rho(x)$, we therefore calculate an average mass density of SiC (ρ_{SiC}) including graphiticlike inclusions (ρ_C). Weighting with the mass fractions c_i, we obtain for the inverse mass density $1/\rho = c_{SiC}/\rho_{SiC} + c_C/\rho_C$. Furthermore, the mass fractions c_i can be expressed by sample composition x in Si_xC: $c_i = m_i/(m_{SiC} + m_C) = x \cdot A_i/(x \cdot A_{SiC} + (1-x) \cdot A_C)$. The resulting mass density is shown by the green line in Fig. 6(a).

Finally, Eq. (1) can be evaluated and reveals the x dependency of $\lambda(x)$, shown in Fig. 6(b). Using this calibration curve together with the measured t/λ profile, presented in Fig. 4, we finally can calculate a depth profile of the Si content in Si_xC for a constant sample thickness of $t = 30$ nm, shown by the cyan curve in Fig. 7. The IMFP plot describes the scenario consistently up to the interface including the buffer layer. The maxima of its oscillatory behavior coincide with the positions of the Si atoms within the SiC matrix. Moreover, we also plotted the Si-EDX and Si-EELS data [from Figs. 3(b) and 3(c)]. The curve coincides very well with the EDX signal and proves indeed a Si depletion within the three topmost SiC bilayers.

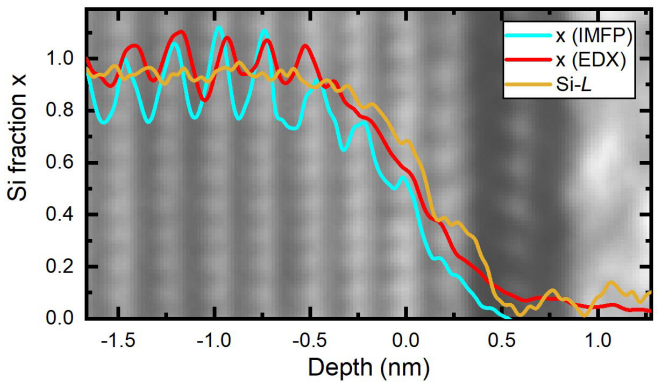

FIG. 7. The depth dependent Si fraction change derived from the IMFP calculation, Si-EDX net intensity, and integral Si-L edge. The depth scale is given with respect to the topmost SiC bilayer.

IV. SUMMARY AND CONCLUSION

In summary, we applied high resolution STEM on epitaxial grown graphene on 6*H*-SiC(0001). Atomically resolved x-ray and EEL spectroscopy allowed us to perform a detailed analysis of the depth dependent substrate composition. In contrast to a widely accepted model of a layer-by-layer decomposition, we reveal a silicon deficiency down to the third bilayer from the surface and a defective substrate down to five bilayers. The Si-vacancy concentration is obviously compensated by the inclusion of C precipitates, which might come along with the build up of strain close to the interface.

Our investigations clearly showed that the interface of epitaxial graphene on 6*H*-SiC(0001) is not atomically sharp. The presence of near-surface defects may not only alter details of the buffer layer bonding but also influence the band alignment across this heterostructure. To what extent these substrate defects can be minimized by more sophisticated sublimation cycling needs further investigations. We also want to emphasize that the defect concentration we showed in this study will depend severely on details of the high temperature processes and the annealing environment. According to the discussion from above, a perfect SiC interface can be reached, if the formation of C clusters within the SiC substrate is suppressed. To what extent this can be reached by improving the heating time and heating ramps needs to be analyzed in more detail.

ACKNOWLEDGMENTS

We thank Dr. M. Dehnert and Prof. R. Magerle from the TU Chemnitz for performing AFM measurements on the TEM lamella structures. We are grateful for the FIB sample preparation performed by Dr. Letian Li.

[1] A. K. Geim, Science **324**, 1530 (2009).
[2] K. S. Novoselov, V. I. Falko, L. Colombo, P. R. Gellert, M. G. Schwab, and K. Kim, Nature **490**, 192 (2012).
[3] P. W. Sutter, J.-I. Flege, and E. A. Sutter, Nat. Mater. **7**, 406 (2008).
[4] X. Li, W. Cai, J. An, S. Kim, J. Nah, D. Yang, R. Piner, A. Velamakanni, I. Jung, E. Tutuc, S. K. Banerjee, L. Colombo, and R. S. Ruoff, Science **324**, 1312 (2009).
[5] A. T N'Diaye, M. Engler, C. Busse, D. Wall, N. Buckanie, F.-J. Meyer zu Heringdorf, R. van Gastel, B. Poelsema, and T. Michely, New J. Phys. **11**, 023006 (2009).

[6] P. Sutter, J. T. Sadowski, and E. Sutter, Phys. Rev. B **80**, 245411 (2009).

[7] C. Wang, W. Chen, C. Han, G. Wang, B. Tang, C. Tang, Y. Wang, W. Zou, W. Chen, X.-A. Zhang, S. Qin, S. Chang, and L. Wang, Sci. Rep. **4**, 4537 (2014).

[8] G. Lippert, J. Dabrowski, T. Schroeder, M. A. Schubert, Y. Yamamoto, F. Herziger, J. Maultzsch, J. Baringhaus, C. Tegenkamp, M. C. Asensio, J. Avila, and G. Lupina, Carbon **75**, 104 (2014).

[9] J. Dabrowski, G. Lippert, J. Avila, J. Baringhaus, I. Colambo, Y. S. Dedkov, F. Herziger, G. Lupina, J. Maultzsch, T. Schaffus, T. Schroeder, M. Kot, C. Tegenkamp, D. Vignaud, and M.-C. Asensio, Sci. Rep. **6**, 31639 (2016).

[10] R. Yekani, E. Rusak, A. Riaz, A. Felten, B. Breitung, S. Dehm, D. Perera, J. Rohrer, C. Rockstuhl, and R. Krupke, Nanoscale **10**, 12156 (2018).

[11] S. K. Lilov, Materials Science and Engineering: B **21**, 65 (1993).

[12] W. Norimatsu and M. Kusunoki, Phys. Chem. Chem. Phys. **16**, 3501 (2014).

[13] G. R. Yazdi, T. Iakimov, and R. Yakimova, Crystals **6**, 53 (2016).

[14] K. V. Emtsev, A. Bostwick, K. Horn, J. Jobst, G. L. Kellogg, L. Ley, J. L. McChesney, T. Ohta, S. A. Reshanov, J. Röhrl, E. Rotenberg, A. K. Schmid, D. Waldmann, H. B. Weber, and T. Seyller, Nat. Mater. **8**, 203 (2009).

[15] M. Kruskopf, D. M. Pakdehi, K. Pierz, S. Wundrack, R. Stosch, T. Dziomba, M. Götz, J. Baringhaus, J. Aprojanz, C. Tegenkamp, J. Lidzba, T. Seyller, F. Hohls, F. J. Ahlers, and H. W. Schumacher, 2D Mater. **3**, 041002 (2016).

[16] D. Momeni Pakdehi, K. Pierz, S. Wundrack, J. Aprojanz, T. T. N. Nguyen, T. Dziomba, F. Hohls, A. Bakin, R. Stosch, C. Tegenkamp, F. J. Ahlers, and H. W. Schumacher, ACS Appl. Nano Mater. **2**, 844 (2019).

[17] T. Cavallucci and V. Tozzini, Sci. Rep. **8**, 13097 (2018).

[18] A. Ouerghi, M. Ridene, C. Mathieu, N. Gogneau, and R. Belkhou, Appl. Phys. Lett. **102**, 253108 (2013).

[19] H. Kageshima, H. Hibino, H. Yamaguchi, and M. Nagase, Jpn. J. Appl. Phys. **50**, 095601 (2011).

[20] G. Sclauzero and A. Pasquarello, Microelectron. Eng. **88**, 1478 (2011).

[21] S. Kim, J. Ihm, H. J. Choi, and Y.-W. Son, Phys. Rev. Lett. **100**, 176802 (2008).

[22] W. Norimatsu and M. Kusunoki, Semicond. Sci. Technol. **29**, 064009 (2014).

[23] I. Shtepliuk, J. Eriksson, V. Khranovskyy, T. Iakimov, A. Lloyd Spetz, and R. Yakimova, Beilstein J. Technol. **7**, 1800 (2016).

[24] X. Weng, J. A. Robinson, K. Trumbull, R. Cavalero, M. A. Fanton, and D. Snyder, Appl. Phys. Lett. **97**, 201905 (2010).

[25] M. Conrad, J. Rault, Y. Utsumi, Y. Garreau, A. Vlad, A. Coati, J.-P. Rueff, P. F. Miceli, and E. H. Conrad, Phys. Rev. B **96**, 195304 (2017).

[26] X. Z. Yu, C. G. Hwang, C. M. Jozwiak, A. Köhl, A. K. Schmid, and A. Lanzara, J. Electron Spectrosc. Relat. Phenom. **184**, 100 (2011).

[27] R. Egerton, R. McLeod, F. Wang, and M. Malac, Ultramicroscopy **110**, 991 (2010).

[28] R. Egerton, Ultramicroscopy **145**, 85 (2014).

[29] C. H. Park, B.-H. Cheong, K.-H. Lee, and K. J. Chang, Phys. Rev. B **49**, 4485 (1994).

[30] L. H. de Lima, A. de Siervo, R. Landers, G. A. Viana, A. M. B. Goncalves, R. G. Lacerda, and P. Häberle, Phys. Rev. B **87**, 081403(R) (2013).

[31] W. Norimatsu and M. Kusunoki, Chem. Phys. Lett. **468**, 52 (2009).

[32] J. Borysiuk, R. Bożek, W. Strupiński, A. Wysmołek, K. Grodecki, R. Stepniewski, and J. M. Baranowski, J. Appl. Phys. **105**, 023503 (2009).

[33] G. M. Rutter, N. P. Guisinger, J. N. Crain, E. A. A. Jarvis, M. D. Stiles, T. Li, P. N. First, and J. A. Stroscio, Phys. Rev. B **76**, 235416 (2007).

[34] A. Mattausch and O. Pankratov, Phys. Rev. Lett. **99**, 076802 (2007).

[35] G. Nicotra, Q. M. Ramasse, I. Deretzis, A. L. Magna, C. Spinella, and F. Giannazzo, ACS Nano **7**, 3045 (2013).

[36] J. D. Emery, B. Detlefs, H. J. Karmel, L. O. Nyakiti, D. K. Gaskill, M. C. Hersam, J. Zegenhagen, and M. J. Bedzyk, Phys. Rev. Lett. **111**, 215501 (2013).

[37] I. Lazic, E. G. T. Bosch, and S. Lazar, Ultramicroscopy **160**, 265 (2016).

[38] D. Perovic, C. Rossouw, and A. Howie, Ultramicroscopy **52**, 353 (1993).

[39] R. D. Leapman and C. R. Swyt, Ultramicroscopy **26**, 393 (1988).

[40] R. Egerton, *Electron Energy-Loss Spectroscopy in the Electron Microscope* (Springer, Verlag, New York, 2011).

[41] S. Schulze, S. Hahn, D. Lehmann, D. Dentel, D. R. T. Zahn, in Book of Tutorials and Abstract of the EMAS2017 Workshop / IUMAS-7 Meeting in Konstanz, Germany, 15th European Workshop, p. 445.

[42] R. H. Packwood and J. D. Brown, X-Ray Spectrometry **10**, 138 (1981).

[43] T. Malis, S. C. Cheng, and R. F. Egerton, J. Electron Microsc. Tech. **8**, 193 (1988).